Journal Name

Combined molecular/continuum modeling reveals the role of friction during fast unfolding of coiled-coil proteins

Alejandro Torres-Sánchez,[a] Juan M. Vanegas,[b] Prashant K. Purohit,[c*] and Marino Arroyo[a,d‡]

Coiled-coils are filamentous proteins that form the basic building block of important force-bearing cellular elements, such as intermediate filaments and myosin motors. In addition to their biological importance, coiled-coil proteins are increasingly used in new biomaterials including fibers, nanotubes, or hydrogels. Coiled-coils undergo a structural transition from an α-helical coil to an unfolded state upon extension, which allows them to sustain large strains and is critical for their biological function. By performing equilibrium and out-of-equilibrium all-atom molecular dynamics (MD) simulations of coiled-coils in explicit solvent, we show that two-state models based on Kramers' or Bell's theories fail to predict the rate of unfolding at high pulling rates. We further show that an atomistically informed continuum rod model accounting for phase transformations and for the hydrodynamic interactions with the solvent can reconcile two-state models with our MD results. Our results show that frictional forces, usually neglected in theories of fibrous protein unfolding, reduce the thermodynamic force acting on the interface, and thus control the dynamics of unfolding at different pulling rates. Our results may help interpret MD simulations at high pulling rates, and could be pertinent to cytoskeletal networks or protein-based artificial materials subjected to shocks or blasts.

1 Introduction

The coiled-coil motif is a prevalent molecular structure that occurs in approximately 10% of all proteins[1,2]. It is composed of 2 to 5 α-helices that wrap around each other to form a super-helix, where hydrophobic amino acids of neighboring chains form a 'zippered' structure in the core of the filament and charged residues on the periphery form stabilizing salt bridges[3–6], see Fig. 1. The most salient mechanical feature of coiled-coils is their ability to sustain large strains along their fibril axis. At strains above $\sim 10\%$, coiled-coils undergo a structural transition in which the α-helices unfold and the coiled-coil structure unwinds[7–9]. This property allows coiled-coils to extend without breaking, and is fundamental for their biological function in various cellular structures.

Coiled-coils are the building block of intermediate fila-

ments[10,11], one of the three major components of the cell cytoskeleton along with microfilaments and microtubules[12]. Intermediate filaments are composed of lateral arrangements of tens of coiled-coils, and create three-dimensional networks that reinforce the cytoplasm[13]. Due to their larger extensibility as compared to microfilaments and microtubules, intermediate filament networks provide a strain buffering element under large deformations (up to 300%) when they are directly loaded under tension[11,14–20]. In these situations, the unfolding of the coiled-coil structure under large stretching may play a major role in the overall cell response[21]. Outside cells, intermediate filaments are found in hair, hoof and wool[22–24]. Coiled-coils also play a key role in motor proteins, such as in Myosin II[5,8,25], where unfolding of the coiled-coil structure is required for optimal mechanical performance[26]. In bioengineering, *de novo* coiled-coils are used as building blocks for the development of new biomaterials, such as fibers[27], nanotubes[28,29], and hydrogels[30,31] to name a few, with potential applications to drug delivery, regenerative medicine and biosensing[4,32].

The unfolding of coiled-coils and other proteins studied by force spectroscopy experiments[8,21,33] and steered molecular dynamics (MD) simulations[34–36] has been rationalized with two-state (folded vs. unfolded) models based on Kramers[37]

[a] *LaCàN, Universitat Politècnica de Catalunya-BarcelonaTech, Barcelona, Spain.*
[b] *Department of Physics, University of Vermont, Burlington, VT 05408, USA*
[c] *Department of Mechanical Engineering and Applied Mechanics, University of Pennsylvania, Philadelphia, PA 19104, USA*
[d] *Institute for Bioengineering of Catalonia, The Barcelona Institute of Science and Technology, 08028 Barcelona, Spain*
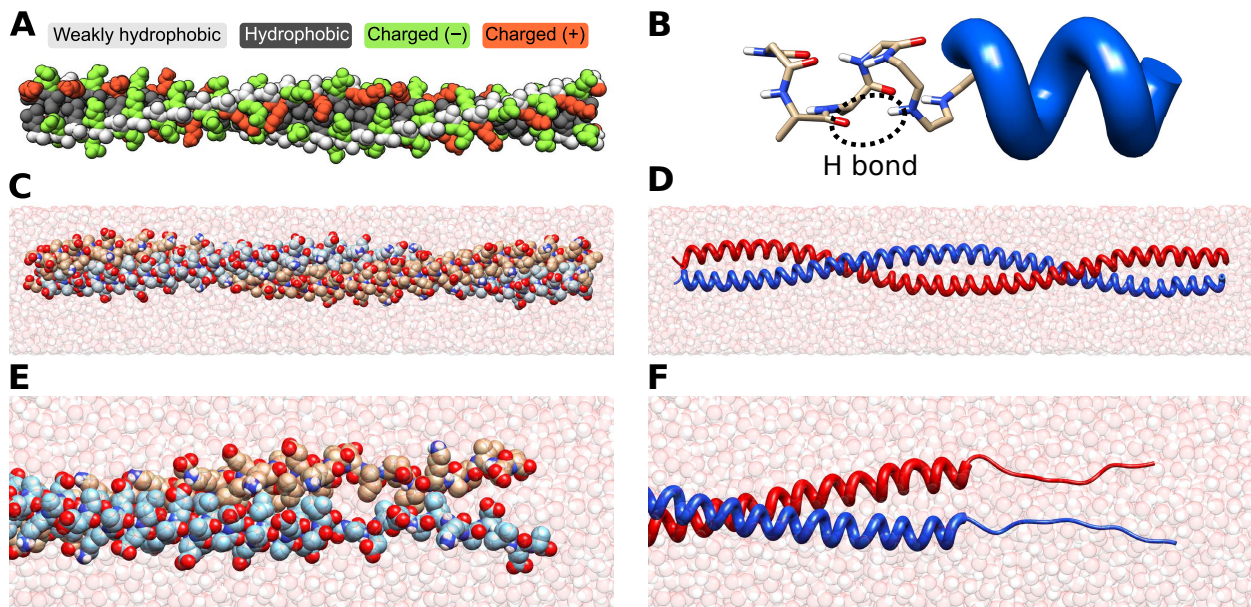[*] purohit@seas.upenn.edu
[‡] marino.arroyo@upc.edu

Fig. 1 (A) Atomistic structure of a coiled-coil protein. A coiled-coil is formed by two right-handed α-helical polymeric chains that adopt a super-helical left-handed structure. (B) Representation of an α-helix showing the hydrogen bonds formed between CO and NH groups (left) that stabilize the helical structure, and ribbon representation (right) showing the polymer backbone of the secondary structure. (C) In our MD simulations, we consider an atomistic description of the coiled-coil with an explicit solvent (waters shown with transparent colors for visualization purposes). (D) Secondary structure of the coiled-coil. The two α-helices wrap around each other to reduce the contact of their hydrophobic sites with the surrounding water. (E) During unfolding, the coiled-coil structrure unfolds due to the rupture of the H-bonds forming the α-helices. This can be better appreciated in the secondary structure (F).

or Bell-Evans theories[38,39]. However, two-state models fail to recapitulate the dynamics of unfolding at different pulling regimes[34,35,40,41]. Deviations between the two-state analysis of non-equilibrium MD simulations and experiments have been attributed to a change in the unfolding mechanism at different pulling rates[34,35]. This problem is further obscured by the usual disparity in pulling rates in experiments (μm/s), and MD simulations (m/s), only bridged in a few works using high-speed force spectroscopy[42]. Here, we show that a simple one-dimensional continuum model of phase-transforming rods, parametrized using all-atom MD simulations, captures the rate-dependent force response naturally, thus extending classical two-state models. A key feature of this framework is the ability to resolve the spatial distribution of forces along the protein. Our results identify a mechanism by which frictional forces with the solvent reduce the driving force on the coiled-unfolded interface at high pulling rates, thus reducing the speed of propagation of the interface.

The regime studied here, in which hydrodynamic interactions affect the force distribution within the fibrous proteins, may be pertinent in various situations. Significant hydrodynamic interactions require very high strain-rates or forces, which in cells can occur during shocks or blasts[43]. Furthermore, the crowded cytosol provides a much more frictional environment than the dilute aqueous solution considered in our MD simulations, and thus lower strain-rates may be sufficient to create significant hydrodynamic forces along the protein. An unfolding coiled-coil protein may also experience a highly frictional environment when bundled in an intermediate filament as it slides relative to adjacent proteins[21], or when a helical strand unfolds while shear-

ing relative to an adjacent one within a coiled-coil protein[44-46]. The regime studied here may also be pertinent to artificial bioinspired materials based on coiled-coils under fast loading rate conditions. Finally, it may provide the background to interpret out-of-equilibrium MD simulations.

The paper is organized as follows. In section 2, we describe the phenomenology of coiled-coil unfolding under force through all-atom MD simulations. In section 3, we present a simple two-state model for the unfolding of coiled-coils parametrized using MD free-energy calculations and show that it can only reproduce the dependence of the rate of unfolding on the applied force for low pulling rates. In section 4, we introduce a one-dimensional continuum mechanics model of phase transforming rods that extends the previous model to deal with higher pulling rates. In section 5, we show numerical simulations of this model and compare them with our MD simulations. We conclude with a summary and discussion of the results.

2 Phenomenology of the unfolding process

To understand the unfolding mechanics of coiled-coils, we perform a series of pulling experiments from MD simulations on a *de novo* coiled-coil based on the amino acid sequence E(IEALKAE)$_{17}$IEA, which is temperature- and chemically-stable[47]. We choose this synthetic coiled-coil because it has a homogeneous structure, in contrast to naturally occurring coiled-coil proteins such as myosin or vimentin, which are inhomogeneous, less stable, and naturally contain weaker regions where the coiled-coil transition nucleates first, such as stutters. Synthetic coiled-coils are aimed at producing more stable and con-
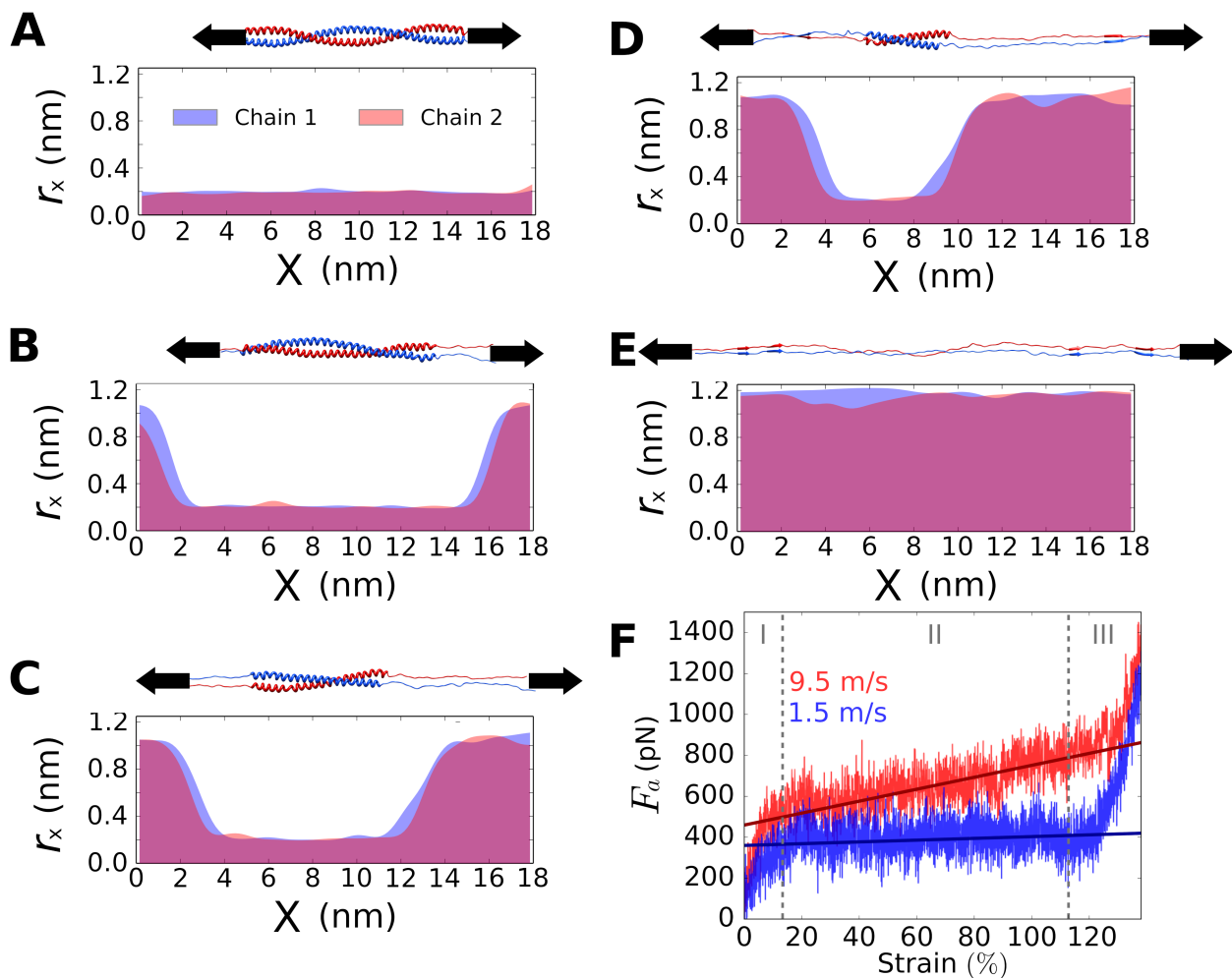
Fig. 2 Phenomenology of unfolding in coiled-coils under force. (A-E) Behavior of r_x along the chain for an experiment at constant pulling velocity $v_p = 1.5$ m/s. After the initial nucleation of small unfolded domains at both ends, the coiled-coil unfolds with two interfaces propagating towards the center. (F) Force-strain relation in experiments at fixed pulling rates. In blue we show the force-strain relation for a simulation at 1.5 m/s. We repeat the procedure for 9.5 m/s (red). We see three regimes where the coiled-coil behaves differently. Regime I shows a linear behavior consistent with the homogeneous stretching of the H-bonds. Regime II presents a plateau typical of the unfolding process, which exhibits a significant slope at high pulling rates. Finally, in regime III we observe a stiffer response with a sharp increase in force as a function of strain, characteristic of the homogeneous stretching of the covalent bonds of the α-helix. In darker blue and red we show the fit to a linear relation of the 1.5 and 9.5 m/s curves respectively in regime II.

trollable structures for bioengineering purposes[4,27,32]. Further details on the molecular composition of this coiled-coil molecule as well as the simulation settings are discussed in Appendix A. Following previous works[34–36,48], we pull from both ends of the protein at a fixed rate. Since the unfolding of coiled-coils is fundamentally driven by the rupture of H-bonds in the α-helices, see Fig. 1, we monitor the lengths of the N_H H-bonds forming the α-helices. More precisely, we monitor their projection onto the fibril axis $\{r_x^i\}_{i=1}^{N_H}$ defined by $r_x = \mathbf{r} \cdot \hat{\mathbf{x}}$, where $\mathbf{r}^i$ is the bond vector of the ith H-bond and the fibril axis is aligned with the x direction. To get a continuous measure, we then calculate $r_x(X,t)$, the field of H-bond distances at time t as a function of the coordinate X, which parametrizes the fibril axis of the coiled-coil in the folded state. Thus, X can be viewed as a Lagrangian coordinate for the system in a fixed reference configuration, the initial folded state at thermodynamic equilibrium and zero force. We obtain $r_x(X,t)$ from $\{r_x^i\}_{i=1}^{N_H}$ by interpolation along the fibril axis using the positions of the H-bonds in the reference configuration.

In Fig. 2 A-E we show the behavior of the protein and $r_x(X,t)$ during a pulling experiment at a constant rate of $v_p = 1.5$ m/s. The chain progressively unfolds, with the coordinated rupture of H-bonds in both α-helices and from both sides of the protein. At low pulling rates, the N terminus (right) of the protein tends to unfold first and this interface initially propagates faster than the interface at the C terminus (left), which is likely due to different inherent stabilities of the helices at two termini. At higher strain rates, we observe other nucleation events occurring randomly along the protein, but the unfolding process is fundamentally driven by the propagation of the primary interfaces at both ends (see supplementary movie). We also note that a steady propagation of the interfaces without refolding events was observed in all pulling experiments tested.

Irrespective of the pulling rate, we observe three different regimes in the force-strain relation during pulling. We define the strain as $\varepsilon = \lambda - 1$ where the stretch $\lambda = l/L$ is the quotient between the deformed and undeformed lengths (Fig. 2 F). At low strains (I) there is a linear dependence between force and strain. During this regime, H-bonds are stretched without rupture. At strains above this maximum value, we observe a crossover above which the force-strain relation exhibits a plateau. This regime (II) with a nearly constant force spans strains up to 120% and corresponds to the progressive unfolding of the coiled-coil protein. For small pulling velocities ($v_p = 1.5$ m/s, blue) the force plateau is nearly constant with a small slope, $F_a = (0.76\varepsilon + 358)$ pN on strain. However, at high pulling velocities ($v_p = 9.5$ m/s, red) this regime exhibits a significant slope, $F_a = (3.02\varepsilon + 450)$ pN, indicative of large dissipation and a highly non-equilibrium process. Finally, when the protein is completely unfolded, we observe again a steep increase in force with the strain, as the covalent bonds in the polymer are stretched (III). Similar force-strain relations are found for naturally occurring coiled-coils, such as myosin[7,8,49], vimentin[13,34], or fibrinogen[48], suggesting that the unfolding of coiled-coils obeys a general principle, regardless of their inner composition[36]. The different regimes can be systematically identified from $r_x(X,t)$. Coiled/unfolded regions can be identified depending on whether $r_x(X,t)$ is lower/higher than a

threshold, e.g. 0.6 nm, and regime II can be assigned to conformations exhibiting coexistence of these two phases.

3 A zipper-like two-state model based on all-atom MD simulations

3.1 Interface propagation based on Arrhenius law

Zipper-like two-state models based on the pioneering works of Gibbs[50,51], Kramers[37] and Bell[38] are widely used to understand the unfolding dynamics of proteins in general[52,53], and coiled-coils in particular[8,21,33–35]. In its simplest version, this model assumes that unfolding occurs in a zipper-like manner with propagating interfaces driven by the consecutive breaking of H-bonds in the protein, in agreement with the observations made in the previous section. At a given force F, the rate at which bonds break is characterized by an Arrhenius law, measuring the rate of change of the fraction of broken bonds

$$k^+(F) = k_0 \exp\left(-\frac{G_b^+(F)}{k_B T}\right), \tag{1}$$

where $G_b^+(F)$ is the energy barrier that bonds need to overcome to break at force F, and k_0 measures the number of attempts that the bond makes to cross the barrier per unit time. The function $G_b^+(F)$ depends on the unfolding mechanism of the phase transition. Equivalently, the rate at which broken bonds reform is given by

$$k^-(F) = k_0 \exp\left(-\frac{G_b^-(F)}{k_B T}\right), \tag{2}$$

where now $G_b^-(F)$ is the energy barrier necessary to reform the bond. Note that since the energy difference between the folded and unfolded states is $\Delta G = G_b^+(F) - G_b^-(F)$, we have

$$\frac{k^+(F)}{k^-(F)} = \exp\left(-\frac{\Delta G(F)}{k_B T}\right), \tag{3}$$

in agreement with detailed balance. At the Maxwell force F_0, $\Delta G(F_0) = 0$, both phases coexist at equilibrium, and the interface does not propagate. The net rate at which unfolding occurs is given by

$$k(F) = k^+(F) - k^-(F)$$
$$= k_0 \left[\exp\left(-\frac{G_b^+(F)}{k_B T}\right) - \exp\left(-\frac{G_b^-(F)}{k_B T}\right)\right]. \tag{4}$$

In this section, we test the validity of Eq. (4) when applied to the unfolding of coiled-coils probed by all-atom MD simulations. For this purpose, we first analyze the free energy profile of the system to obtain $G_b^\pm(F)$. Then, we perform a set of pulling experiments for a wide regime of pulling rates and forces. For each experiment, we measure k and F and check whether Eq. (4) is satisfied.

3.2 Free energy profile

To compute the free energy barriers $G_b^\pm(F)$ relevant to the unfolding of coiled-coils, we resort to the free energy landscape of the

protein in terms of a collective variable capturing protein elongation. We note that doing this involves a significant conceptual step, since we use an equilibrium free energy surface to predict the out-of-equilibrium unfolding of the protein. One can only expect reasonable results close enough to equilibrium in line with Onsager's linear response theory[54–56]. We thus first calculate the free energy profile of the protein in terms of meaningful collective variables (CVs). We already noted that unfolding is mainly characterized by (1) the breaking of H-bonds of the α-helices forming the super-coil, and (2) the unwinding of the coiled-coil. From these two processes, the rupture of H-bonds dominates the kinetics of unfolding[34]. Thus, a collective variable that characterizes the state of the coiled-coil protein is the average of the projection of the H-bond distance onto the fibril axis

$$\langle r_x \rangle = \frac{1}{N_H} \sum_i r_x^{(i)}. \tag{5}$$

While $\langle r_x \rangle$ characterizes the degree of stretching of the protein, it cannot determine if the stretching is homogeneous, so that all H-bonds are uniformly strained, or inhomogeneous as the result of a mixture of coiled and unfolded phases. To properly sample the system and build a meaningful free energy landscape, which should depend not only on the degree of stretching but also on the heterogeneity of stretching, we follow Samuelson et al.[57] and add the standard deviation of r_x as an auxiliary CV

$$\sigma_{r_x} = \sqrt{\langle r_x^2 \rangle - \langle r_x \rangle^2}. \tag{6}$$

For $\sigma_{r_x} \approx 0$ the chain is homogeneously elongated, whereas when this quantity increases, the system can develop heterogeneities.

To analyze the free energy lanscape $A(\langle r_x \rangle, \sigma_{r_x})$, we use well-tempered metadynamics[58] with multiple walkers[59], as implemented in the PLUMED package[60]. In this methodology, the system is analyzed in parallel with multiple random walkers in the collective-variable space at temperature fT, which allows the system to overcome energy barriers that are practically inaccessible at the original temperature T. The free energy landscape at temperature fT is then appropriately reweighted to recover the free energy landscape at the original temperature T. Here, we employed 200 walkers simultaneously at $T = 310$ K and $f = 20$. We let the walkers sample the collective variable space until the free energy landscape becomes stationary, which determines the criterion for convergence.

In Fig. 3I we show the converged free energy landscape resulting from this analysis. There are two main energy wells corresponding to the coiled state, $\langle r_x^{co} \rangle = 0.198$, and the unfolded state, $\langle r_x^{un} \rangle = 0.828$. The well of the coiled state is narrower and more stable, and is characterized by a small standard deviation σ_{r_x}. In contrast, the unfolded state has a wider well with higher energy (21 kJ/mol) and higher σ_{r_x}, characteristic of its random-polymer nature. One can define a minimum energy path between these two minima (A-E). States that deviate from this path are penalized due to a smaller or higher σ_{r_x} (F and G), which induce unfavorably homogeneous or heterogeneous unfolding states. Upon further stretching, the coiled-coil gets straightened but with a significant free energy cost (H). Integration of the free energy surface along σ_{r_x},

$$A(\langle r_x \rangle) = -k_B T \log \int e^{-A(\langle r_x \rangle, \sigma_{r_x})/k_B T} d\sigma_{r_x}, \tag{7}$$

results in an effective free energy profile in terms of $\langle r_x \rangle$ only (Fig. 3II black) at zero force.

The main outcome of this free energy calculation is a profile that clearly identifies two low-energy states, folded and unfolded, and quantifies the barrier. We note that the partially folded intermediates sampled by the metadynamics algorithm (Fig. 3B-D, F,G) are very unlikely conformations required to quantify the heigh of the barrier in thermodynamic equilibrium, and thus not representative of the mechanism during the sequential unfolding observed in our out-of-equilibrium simulations. Ultimately, the free energy calculation provides a thermodynamic characterization of an elementary unfolding step.

With the free energy landscape at zero force at hand, we need to couple F with our measure of extension, $\langle r_x \rangle$, to account for the induced tilting of free energy, and hence to compute the energy barriers as a function of force. First, we note that the force is equally shared by the two α-helices. Since H-bonds are tension loaded during unfolding, the force along the fibril axis on each H-bond is $F/2$ on average. In other words, the thermodynamic conjugate of $\langle r_x \rangle$ is $F/2$. Therefore, the driving free energy during unfolding is

$$G(\langle r_x \rangle, F) = A(\langle r_x \rangle) - \frac{1}{2} F \left(\langle r_x \rangle - r_{x,co} \right), \tag{8}$$

which tilts the free energy by the force application about the coiled ground state. In Fig. 3II, we plot $G(\langle r_x \rangle, F)$ for different values of F. We observe that at $F_0 = 113$ pN the coiled and unfolded states have the same energy. At higher forces, the unfolded state becomes the most stable equilibrium configuration. We can obtain $G_b^{\pm}(F)$ by direct examination of the energy barriers of $G(\langle r_x \rangle, F)$. The functions $G_b^{\pm}(F)$ are in general non-linear functions of F, since the positions of the minima and maxima change with the force, but this effect is small and they can be accurately linearized around F_0 (see Table 1).

3.3 Comparison with MD simulations

We now examine whether the two-state model based on the Arrhenius law in Eq. (4) and the barriers $G_b^{\pm}(F)$ estimated from the equilibrium free-energy profile reproduces the unfolding of coiled-coils in our MD simulations. For that, we first consider a set of pulling experiments at constant force and evaluate $G_b^{\pm}(F)$ as discussed in the previous section. To calculate the rate of unfolding k in the simulation, we establish the relation between k and $\langle \dot{r}_x \rangle$, where the over-dot denotes time derivative. We first note that the average H-bond distance, $\langle r_x \rangle$, can be expressed in terms of the average H-bond distances of broken $\langle r_x \rangle_{un}$, and intact, $\langle r_x \rangle_{co}$, H-bonds

$$\alpha_{un} \langle r_x \rangle_{un} + \alpha_{co} \langle r_x \rangle_{co} = \langle r_x \rangle, \tag{9}$$

where α_{un} and α_{co} are the fractions of broken and intact H-bonds. The quantities $\langle r_x \rangle_{un}$ and $\langle r_x \rangle_{co}$ are approximately constant dur-
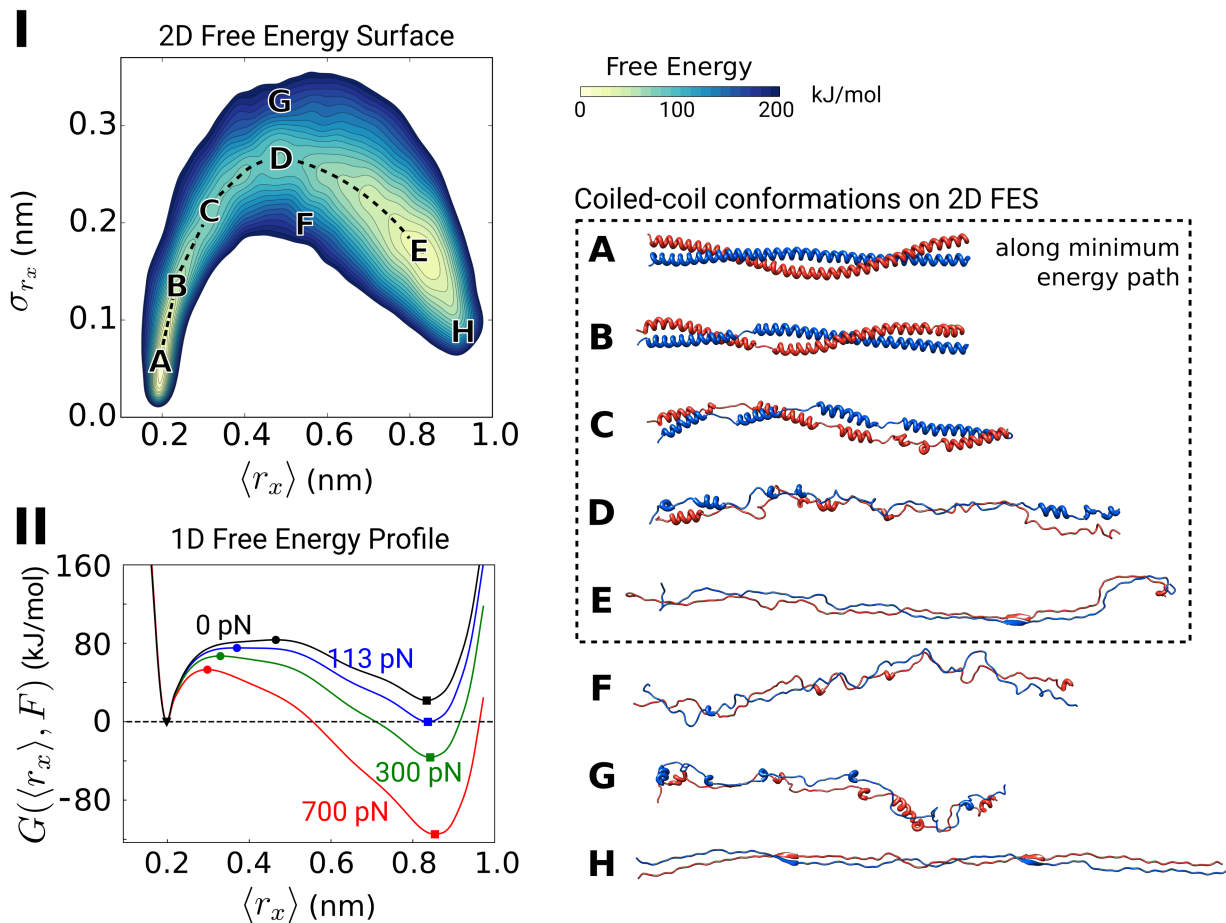
Fig. 3 Analysis of the free energy landscape. (I) Free energy surface in terms of $\langle r_x \rangle$ and σ_{r_x}. Representative states in the free energy surface (A-H) are shown to illustrate the behavior of the coiled-coil along the free energy surface. States A-E follow the minimum energy path between the coiled-coil state (A) and the unfolded state (E). (II) Free energy profile $G(\langle r_x \rangle, F)$ for different forces F in terms of $\langle r_x \rangle$. In each curve the triangles, squares and circles indicate the positions of the coiled minimum, the unfolded minimum and the maximum respectively. At zero force (black), we obtain $A(\langle r_x \rangle)$ by integration of $A(\langle r_x \rangle, \sigma_{r_x})$ along σ_{r_x} (Eq. (7)). At the critical force, $F_0 = 113$ pN (blue), the two coiled and unfolded states have the same energy. At higher forces (green, red), the unfolded state is energetically favorable.

ing the unfolding process. Taking into account that $\alpha_{co} = 1 - \alpha_{un}$, we obtain

$$\dot{\alpha}_{un}\left(\langle r_x \rangle_{un} - \langle r_x \rangle_{co}\right) = \langle \dot{r}_x \rangle, \tag{10}$$

and thus,

$$k = \dot{\alpha}_{un} = \frac{\langle \dot{r}_x \rangle}{\left(\langle r_x \rangle_{un} - \langle r_x \rangle_{co}\right)}, \tag{11}$$

where we have assumed that there are two propagating interfaces. It is clear from this expression that k measures the rate of change of the fraction of broken H-bonds.

We now examine the relation between k and $G_b^+(F)$ in MD simulations. Because we are not interested in the initial elastic loading of the molecule, we start with a configuration where unfolded sections near the two ends have already nucleated. Assuming that the interface velocity obeys the Arrhenius law in Eq. (4), and taking into account that for the range of forces we are examining $G_b^-(F) \gg G_b^+(F)$, we have

$$k(F) \approx k_0 e^{-G_b^+(F)/k_B T}. \tag{12}$$

Therefore, if the effective kinetic law underlying the unfolding process in our MD simulations was indeed given by an Arrhenius law, then $\log(k(F))$ should be linearly related to $G_b^+(F)$, with a slope of $\beta = -1/k_B T$ and a zeroth order term given by $\log(k_0)$. In Fig. 4A, we show the data obtained from simulations at different pulling forces, and the fit to an Arrhenius law with $k_0 = (3.8 \pm 0.1) \times 10^9 \text{ s}^{-1}$. We note that β is not a fitting parameter and is kept to its nominal value given by the thermostat ($T = 310$ K) of our molecular dynamics simulations. Thus, the simulations agree remarkably well with a two-state model based on an Arrhenius law and on an estimation of energy barriers based on the equilibrium free energy for low forces ($170 < F < 410$ pN).

We now examine the relation between k and F for higher pulling forces. In Fig. 4B, we plot k as a function of F according to the data in our MD simulations for low (blue circles) and high (red squares) forces. We compare this data with the theoretical expression in Eq. (12) encoding Arrhenius law, where $G_b^+(F)$ is computed from the free-energy profile and k_0 is fitted as from Fig. 4A as described above (dashed curve). As in Fig. 4A, we observe an excellent agreement between theory and MD data at low forces (blue circles), whereas at high forces (red squares) the deviation becomes very significant. This distinction between the low-force and high-force regimes is also apparent at constant pulling rates (yellow triangles), where the force is calculated as the average force in the plateau regime. The data that corresponds to the simulations in Fig. 2 are marked with double triangles for reference.

Thus, our simulations closely follow the predictions of a two-state model based on an Arrhenius law for low pulling forces and rates, but they clearly deviate from it at high pulling forces or fast rates. To explain this discrepancy in highly out-of-equilibrium situations, we hypothesize that hydrodynamic interactions between the unfolding molecule and the surrounding solvent may play a role, since such friction in principle reduces the force that effectively acts at the interface. Microscopically, fast processes preclude full relaxation of the protein and the solvent, lead to rate-

dependent entropy production and energy dissipation, which can be lumped within Onsager's linear response theory into an effective friction coefficient as discussed below[55,56]. If this hypothesis was true, the anomalous behavior at high pulling rates would not respond to a breakdown of Arrhenius law or to a switch in the unfolding mechanism as previously hypothesized[34,35,40,41], but to a reduction of the applied force caused by hydrodynamical interactions. In support of this hypothesis, we note that all-atom simulations using implicit solvent[36], and thus missing any hydrodynamic effect, showed a higher plateau at higher pulling rates, but did not exhibit the increasing slope in region II that we observe in our explicit solvent simulations at high pulling rates, see Figure 2. Similarly, a theoretical model describing the progressive unfolding of a fibrous protein but ignoring hydrodynamic effects predicted a higher plateau at high pulling velocities, albeit with zero slope[53].

To test this hypothesis, we describe next a theoretical model accounting for the force distribution along a phase-transforming rod in the presence of a viscous frictional interaction with the environment.

4 A continuum model of phase-transforming rods

To examine the role of viscous friction during fast unfolding of coiled-coils, we model the protein as a one-dimensional phase-transforming continuum rod. This framework has been previously used to rationalize materials exhibiting phase transitions including rod-like macromolecules such as DNA[61,62] or beam-like nanoscale materials such as multi-walled carbon nanotubes[63]. It has also been applied to the α-helix to β-sheet transition in muscle protein titin[64] or in the whelk egg capsule biopolymer[65,66]. Recently, this approach has been used to understand steered MD simulations of coiled-coils under a negligible frictional force[36]. Let us briefly discuss the basic ingredients of this continuum model.

We represent by $\varphi_t(X)$ the deformation mapping at time t such that, at $t = 0$, $\varphi_0(X) = X$. We denote by $F(X,t)$ the force acting on this material particle and by $F_a = F(0) = F(L)$ the force applied at the ends. We consider that there are two propagating interfaces, one for each end of the protein, between coiled and unfolded phases, parametrized by their position in the reference configuration $S_1(t)$ and $S_2(t)$ respectively. Thus, $s_1(t) = \varphi_t(S_1(t))$ and $s_2(t) = \varphi_t(S_2(t))$ are the positions of the interfaces in the deformed configuration at time t, see Fig. 5. If we model the system as an overdamped rod in a frictional medium approximating a Newtonian fluid, conservation of linear momentum for this system along the fibril axis reads

$$\frac{\partial F}{\partial X} = \eta v, \tag{13}$$

where $v = \partial \varphi / \partial t$ and η is the effective drag coefficient for the coiled-coil protein in the surrounding viscous fluid[67]. In principle, η could depend on whether the protein is locally coiled or unfolded, leading to two coefficients η_{co} and η_{un}. However, here we assume that both coefficients are equal. We model the elastic-
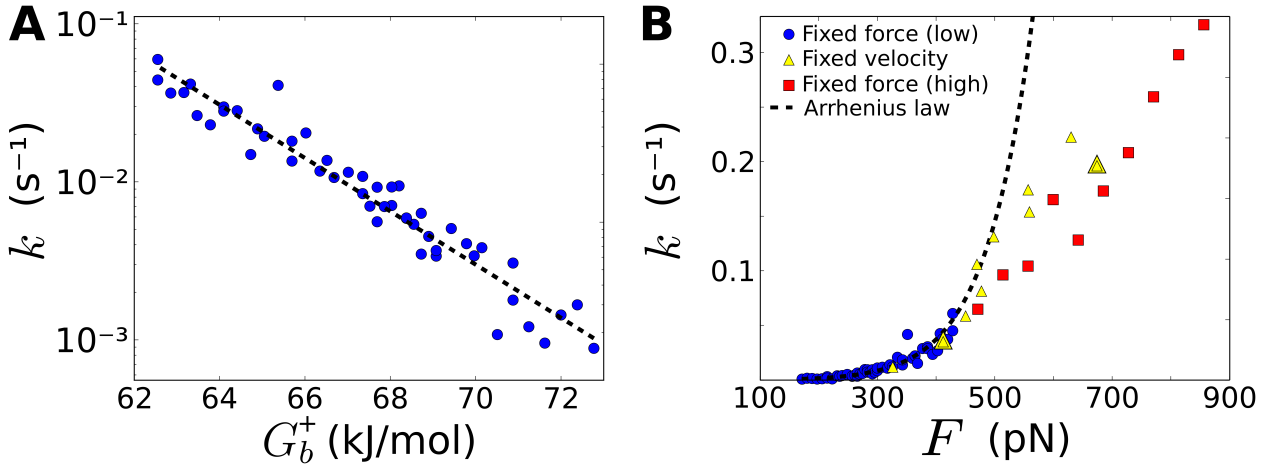
Fig. 4 Predictions of the two-state model based on an Arrhenius law for a single propagating interface. (A) Interface velocity versus Gibbs energy barrier $G_b^+(F)$ for experiments at constant low forces ($F < 410$ pN) represented in blue. In this regime, unfolding follows an Arrhenius law (dashed line) characterized by an exponential dependence of the interface velocity in terms of the Gibbs energy barrier, which is in turn a function of the applied force F. (B) Interface velocity versus F. The Arrhenius law fails to predict the behavior of the unfolding for higher forces (red). The same kind of behavior is observed in simulations performed at constant velocities (yellow).
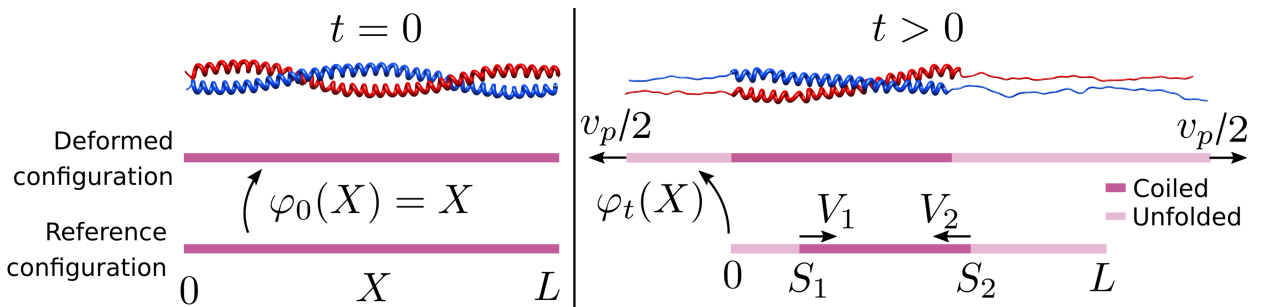

Fig. 5 A one-dimensional continuum model for coiled-coil unfolding based on phase-transforming rods. Initially, the coiled-coil is at equilibrium in the coiled state, which defines the reference configuration in our continuum mechanics model (left panel). We then a pull at two ends of the coiled-coil at rate v_p. The deformed configuration of the coiled-coil at time t is given by the deformation mapping $\varphi_t(X)$, which maps a point X in the reference configuration onto the deformed configuration. In this deformed configuration, part of the coiled-coil protein has unfolded. To track the phase transformation, we identify the position of the interfaces between the coiled and the unfolded phases in the reference configuration by the time-dependent variables $S_1(t)$ and $S_2(t)$. Their positions in the deformed configuration are given by $s_1 = \varphi_t(S_1(t))$ and $s_2 = \varphi_t(S_2(t))$. The rate of change of $S_1(t)$ and $S_2(t)$, $V_1 = dS_1/dt$ and $V_2 = dS_2/dt$, follow the Arrhenius law Eq. (4).

ity of the rods with a force-strain relation given by

$$F(X,t) = \begin{cases} k_{co}\varepsilon(X,t) & \text{if } X \le S(t) \\ k_{un}\left[\varepsilon(X,t) - \varepsilon_{un}^0\right] & \text{if } X > S(t), \end{cases} \quad (14)$$

where $\varepsilon = \partial_X \varphi_t - 1$ is the local strain, k_{co} is the elastic constant in the coiled state, and k_{un} and ε_{un}^0 are the elastic constant and the equilibrium strain for the unfolded state, respectively.

Assuming that the rate of unfolding is characterized by an Arrhenius law, we can write

$$\dot{S}_i = \frac{L}{2}k(F(S_i)), \quad i = 1,2 \quad (15)$$

where $k(F)$ is given by the Arrhenius expression Eq. (4). Note from this expression that if the fraction of unfolded bonds α_{un} becomes 1 in a unit time, then $k = 1$ and two interfaces would have traveled at a velocity $S_i = L/2$ as expected. If ηv is small, such as for small pulling rates, then $\partial F/\partial X \approx 0$ and therefore F is approximately constant. In that situation, $F(S_i) \approx F_a$ and we recover the two-state model.

Interestingly, these equations can be derived following a variational framework, called Onsager's formalism[54,56,68], see Appendix B. This variational principle sheds light into the dissipative structure of the problem. For instance, one can identify the net dissipation of the system as

$$\mathscr{D} = \int_0^L \eta v^2\, dX + \frac{1}{\bar{\kappa}_1}\dot{S}_1^2 + \frac{1}{\bar{\kappa}_2}\dot{S}_2^2, \quad (16)$$

where

$$\bar{\kappa}_i = k_0 \frac{\exp\left(-\dfrac{G_b^+\left(F(S_i)\right)}{k_B T}\right) - \exp\left(-\dfrac{G_b^-\left(F(S_i)\right)}{k_B T}\right)}{\varepsilon_{un}^0 F(S_i) - \Delta a}, \quad (17)$$

F_{S_i} identifies the force at the interfaces, and $\Delta a = \varepsilon_{un}^0 F_0$ measures the difference in free energy densities between the coiled and unfolded phases at equilibrium. Eq. (16) clearly identifies the two different dissipation mechanisms of unfolding, namely friction with the solvent (the integral term on the left) and propagation of the interfaces, each playing a dominant role depending on the pulling rate as discussed in section 5.2. This differs from classical two-state models, where only interface propagation dissipates energy.

To properly describe our continuum model, we need to find the elastic constants k_{co}, k_{un} of the protein, the equilibrium strain in the unfolded state ε_{un}^0, and the friction coefficient η. So far we have characterized the stretching of the coiled-coil protein through H-bond distances. While H-bond distances are good descriptors for unfolding of the protein, they do not properly describe the elastic stretching, which also depends on the elongation of other structures of the chain. For this reason, it is not possible to obtain good measures for the elastic constants of each phase from the free energy profile shown in Fig. 3II. To calculate the elastic constants of the model, we consider pulling experiments at constant pulling rate v_p for low pulling rates $v_p < 2$ m/s so that the effect of friction is negligible. In that case, the force-strain curve in the coiled and unfolded phases looks like a straight line

whose slope is precisely k_i with an offset that provides ε_{un}^0 for the unfolded regime. We find that $k_{co} = 4.4 \times 10^3$ pN, $k_{un} = 5.0 \times 10^3$ pN and $\varepsilon_{un}^0 = 1.15$. The friction coefficient is estimated below.

5   Results of the continuum model

In this section, we test the validity of our atomistically-informed continuum model against MD simulations and examine the role of friction. Then, we compute the energy dissipated during unfolding, an important measure to understand the function of coiled-coils at different pulling regimes. Details of the numerical simulations of the continuum mechanics model are described in Appendix C.

5.1   Comparison with MD simulations

We validate here our continuum model by comparing the force-strain relation under a fixed pulling rate with the results from MD simulations. Before proceeding, we need to find the friction coefficient in our model. To show the effect of the friction coefficient in the force-strain relation, we examine the dynamics of the continuum model at a pulling rate of 9.5 m/s with different friction coefficients and compare them against a MD simulation, see Fig. 6A. We observe that the friction coefficient controls the slope of the plateau during the unfolding process, whereas it has a much smaller effect in regimes I and III. For a vanishing friction coefficient, the results of a two-state model with a vanishing slope at the plateau are recovered. In view of this, the friction coefficient is estimated by adjusting the slope during regime II. We find that $\eta = 8$ pN·ns/nm^2 predicts well the slope of the plateau for all pulling rates tested, see Fig. 6B.

We now examine the force distribution $F(X)$ at different stages of the dynamics for continuum simulations with fixed applied velocity or force. Note that, since our continuum model does not contain any symmetry-breaking ingredient, both ends of the molecule unfold with the same speed towards the center, which remains stationary. For fixed pulling rates (Fig. 7A), we observe that the force decays almost linearly from the ends, where $F(0) = F(L) = F_a$, to the interfaces, where $F(S_1) = F(S_2) = F_i$. This linear variation, in the light of Eq. (13), suggests that the unfolded region moves as a rigid (yet growing) body with the imposed velocity v_p. We observe that F_i is approximately constant throughout the time-evolution for the three pulling experiments. In contrast, F_a presents a larger time-dependence, particularly at higher pulling rates. This figure contains the most relevant result of this paper, namely that friction attenuates the force applied on the molecule and leads to a smaller force at the interface, where the Arrhenius law applies. For experiments at constant F_a (see Fig. 7B), we observe again a linear decay of the force in the unfolded region. At higher forces ($F_a = 800$ pN) we observe that the force in the coiled region is not constant initially (darkest red curve), which suggest that unfolding started before the force was transmitted throughout the initially coiled molecule in a highly non-equilibrium process. Remarkably, the constant pulling-rate protocol (Fig. 7A) results in a highly constant force at the interface, even though the force at the ends, F_a, changes during the unfolding process.
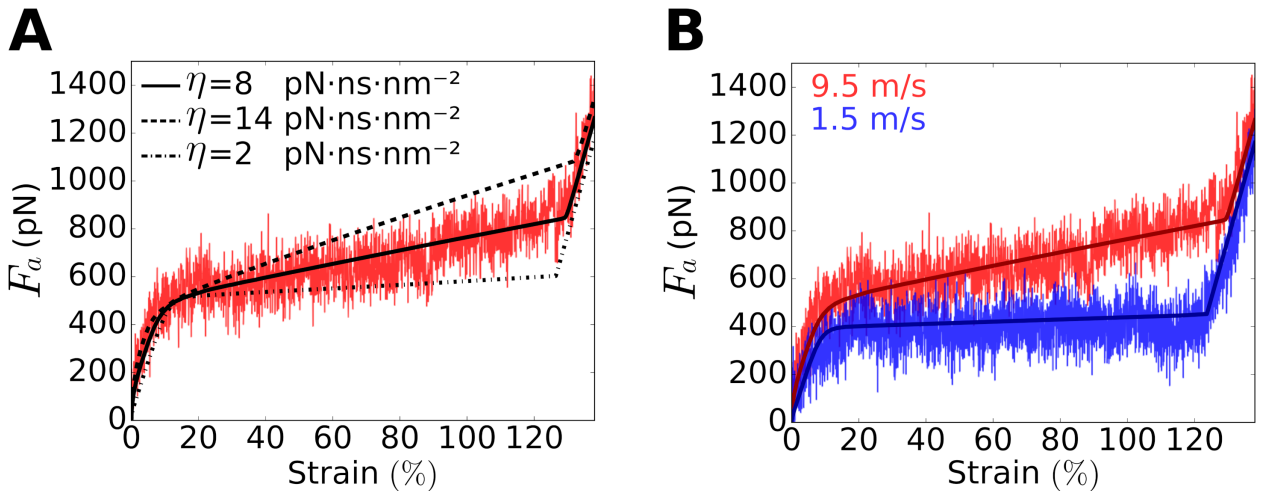
Fig. 6 (A) Comparison between a MD simulation at 9.5 m/s and continuum simulations with different friction coefficients, which shows that the slope of the force-strain relation at the plateau from MD simulations can be used to determine the friction coefficient in the model. (B) Comparison between the force-strain relation in MD and continuum simulations for two different pulling rates 1.5 m/s (blue) and 9.5 m/s (red).

Let us now revisit the validity of Arrhenius law for higher forces and pulling rates. Given the applied force F_a or the stretching velocity v_p, our continuum simulations allow us to estimate the force at the interface F_i accounting for friction with the environment, which should govern the velocity of the interface, or equivalently k. Thus, we can use this information to infer F_i from the values of F_a or v_p of our MD simulations and re-plot Fig. 4B in terms of F_i. However, F_i changes during the unfolding process, particularly in constant F_a simulations. We note, however, that the change in F_i during unfolding is small compared to the difference between F_a and F_i. Thus, to a good approximation we can consider F_i to be constant, and equal to its average value during unfolding. Figure 7C tests the Arrhenius law in our MD simulations accounting for this correction. Remarkably, we observe an excellent agreement between the MD data and the Arrhenius law, even for high propagation speeds, provided that the correct force at the interface is used. This agreements also reflects in an accurate prediction by the continuum model of the relation between the extension rate of the protein and the force during the plateau, see Figure 7D.

In summary, our continuum model reproduces well MD simulations, even for higher forces and pulling rates, where conventional two-state models fail. We have shown that: 1) friction plays a critical role at higher pulling forces and rates by reducing the actual force at the interface driving its motion, 2) the friction coefficient can be estimated from the slope of regime II obtained from MD simulations, and 3) friction leads to a non-trivial force distribution along the protein, which can be computed using our atomistic-based continuum model. One could in principle measure $F(X)$ from non-equilibrium MD simulations, e.g. using microscopic stress calculations[69,70]. However these measures are computationally expensive and require significant temporal and spatial smoothing. In contrast, our continuum approach provides a means to infer the force distribution along the protein from a simple atomistically-informed continuum calculation.

5.2 Energy dissipation

Coiled-coils have been reported to unfold as truly elastic materials with negligible energy dissipation[8], but also as strain buffering elements that dissipate large quantities of energy and provide a means to absorb energy in shocks[34]. As we show next, our theoretical model reconciles these behaviors because coiled-coils dissipate energy during unfolding in a rate-dependent fashion, which allows them to act both as elastic materials at low pulling rates, and as highly dissipative elements at higher pulling rates. This dual behavior is essential for the biological function of coiled-coils in different cell structures such as intermediate filaments or myosin motors[1,7,8,34]. While Eq. (16) provides a route to compute the energy dissipated during the unfolding process, this expression is difficult to exercise in MD simulations, since one would need to compute the velocity field along the protein. To estimate the energy dissipated during protein unfolding, we evaluate the work input to the system due to the applied force F_a when stretching the coiled-coil from an initial homogeneous strain ε_0 to a strain ε_1,

$$W(\varepsilon_0, \varepsilon_1; v_p) = L \int_{\varepsilon_0}^{\varepsilon_1} F_a(\varepsilon; v_p) d\varepsilon$$

$$= \Delta A(\varepsilon_0, \varepsilon_1) + Q(\varepsilon_0, \varepsilon_1; v_p), \quad (18)$$

which can be split into the free energy stored by the coiled-coil, $\Delta A(\varepsilon_0, \varepsilon_1)$ and heat, $Q(v_p)$, which represents the energy dissipated in the process due to friction. Assuming that after unfolding the strain is also homogeneous, which holds approximately true for all simulations, the change in free energy $\Delta A(\varepsilon_0, \varepsilon_1)$ is independent of v_p and can be calculated from

$$\Delta A(\varepsilon_0, \varepsilon_1) = L \int_{\varepsilon_0}^{\varepsilon_1} F_{eq}(\varepsilon) d\varepsilon, \quad (19)$$

where $F_{eq}(\varepsilon)$ is the force on the coiled-coil at equilibrium for a given strain ε. As discussed earlier, the equilibrium force exhibits
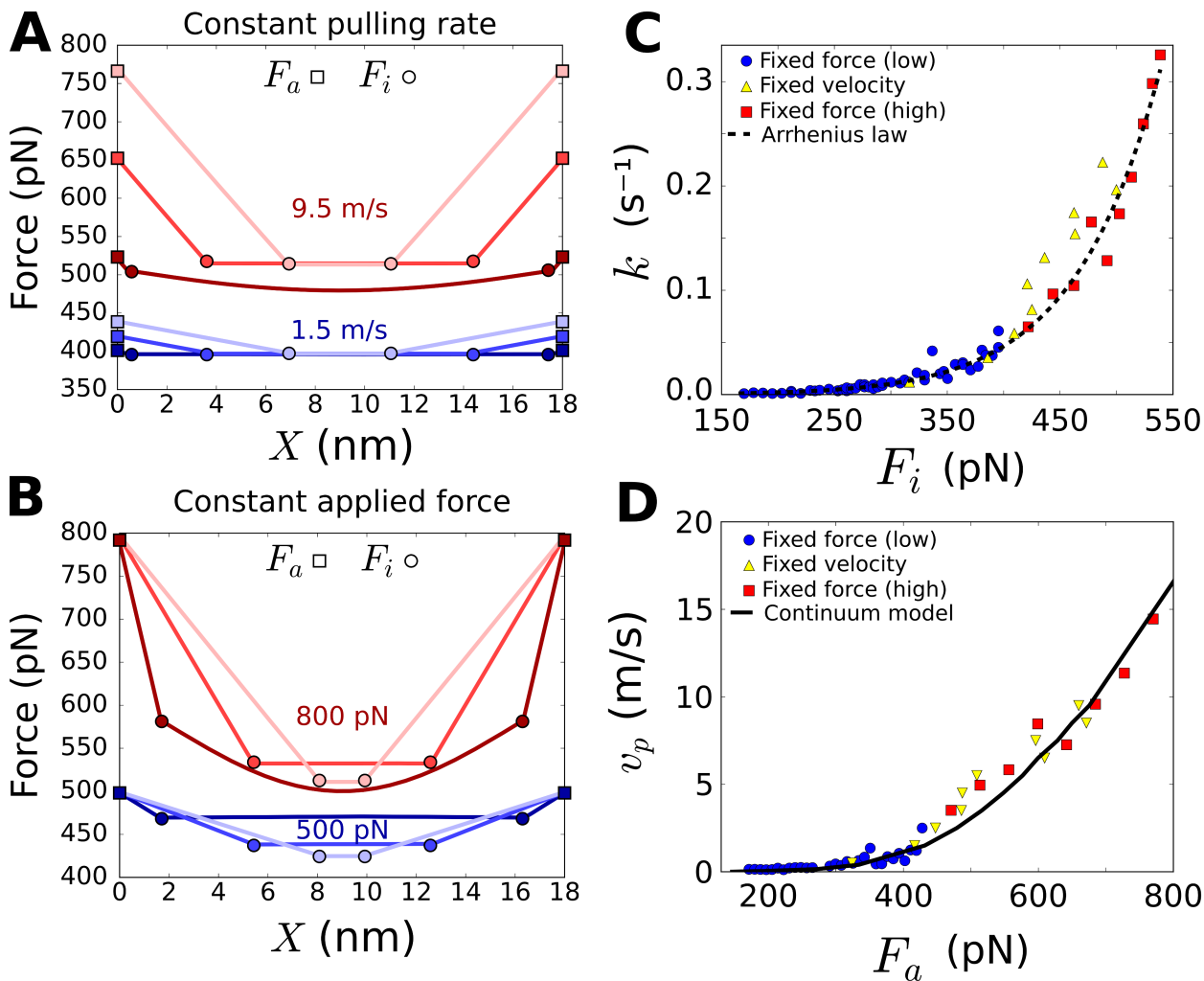
Fig. 7 (A) Force distribution $F(X)$ for two continuum simulations at constant pulling rates $v_p = 1.5$ m/s (blue) and $v_p = 9.5$ m/s (red) at three different stages of the unfolding dynamics (darker to lighter colors). The applied force F_a and the force at the interface F_i are marked with squares and circles respectively. (B) Force distribution for two continuum simulations at constant applied force $F_a = 500$ pN (blue) and $F_a = 800$ pN (red) at three different stages of the unfolding dynamics (darker to lighter colors). (C) Arrhenius law in terms of the actual force at the interface F_i accounting for friction with the environment and comparison with the MD simulations in Fig. 4B, where now we observe an excellent agreement even at higher pulling forces and rates. (D) Extension rate of the protein as a function of the force at the ends during the unfolding regime (II) for all the MD simulations at constant strain-rate and force, and predicted relation by the continuum model.
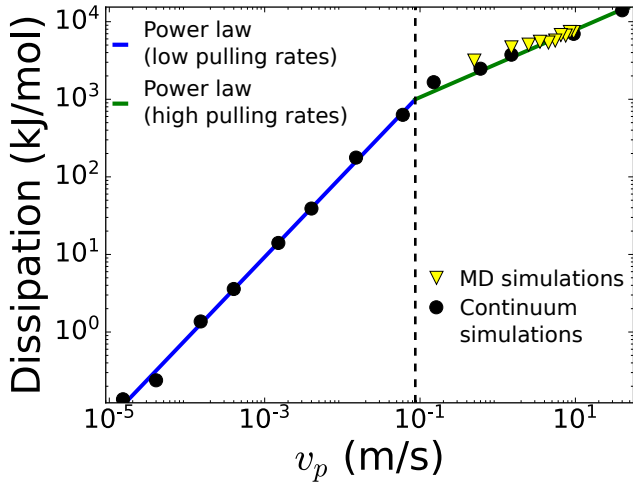
Fig. 8 Energy dissipated as a function of the pulling rate v_p in a log-log plot. Yellow triangles represent the MD pulling experiments in Fig. 4 while black dots are obtained from our continuum mechanics model. We observe an excellent agreement between both. The continuum mechanics model allows exploration of very low pulling rates, which are well beyond the accessible timescales from MD simulations. The energy dissipated can be described by two power laws (linear relations in the log-log plot), that present a crossover at $v_p \approx 0.1$ m/s (see the main text).

three regimes

$$F_{\text{eq}}(\varepsilon) = \begin{cases} k_{\text{co}}\varepsilon & \text{if } \varepsilon \leq \hat{\varepsilon}_{\text{co}} \\ F_0 & \text{if } \hat{\varepsilon}_{\text{co}} < \varepsilon < \hat{\varepsilon}_{\text{un}} \\ k_{\text{un}}(\varepsilon - \varepsilon_{\text{un}}^0) & \text{if } \varepsilon \geq \hat{\varepsilon}_{\text{un}} \end{cases}, \qquad (20)$$

where

$$\hat{\varepsilon}_{\text{co}} = F_0/k_{\text{co}} \qquad \hat{\varepsilon}_{\text{un}} = \varepsilon_{\text{un}}^0 + F_0/k_{\text{un}}. \qquad (21)$$

Thus, we can compute the energy dissipated in the process as

$$Q(\varepsilon_0, \varepsilon_1; v_p) = W(\varepsilon_0, \varepsilon_1; v_p) - \Delta A(\varepsilon_0, \varepsilon_1). \qquad (22)$$

Fixing $\varepsilon_0 = 0$ and $\varepsilon_1 = 130\%$, we evaluate $Q(\varepsilon_0, \varepsilon_1; v_p)$ both for MD (yellow triangles) and continuum simulations (black dots) as shown in Fig. 8. The observed agreement between the MD and continuum models is remarkable. We note that changing ε_0 and ε_1 such that $\varepsilon_0 < \hat{\varepsilon}_{\text{co}}$ and $\varepsilon_1 > \hat{\varepsilon}_{\text{un}}^0$ affects only marginally $Q(\varepsilon_0, \varepsilon_1; v_p)$, which suggests that most of the dissipation occurs during unfolding (data not shown). For that reason, we simply write $Q(v_p)$ to denote $Q(\varepsilon_0, \varepsilon_1; v_p)$. Interestingly, we observe two different regimes for $Q(v_p)$, which are characterized by power laws in terms of v_p and present a crossover at $v_p^* = 0.087$ m/s

$$Q(v_p) = \begin{cases} \left(\dfrac{v_p}{v_1}\right)^m & \text{if } v_p \leq v_p^* \\ \left(\dfrac{v_p}{v_2}\right)^n & \text{if } v_p > v_p^* \end{cases}, \qquad (23)$$

where $m = 1.06$, $n = 0.39$, $v_1 = 1.14 \times 10^4$ m/s and $v_2 = 8.62 \times 10^{-10}$ m/s. For a pulling rate of v_p^*, the average applied force in the plateau is $F_a^* \approx 150$ pN. The change of behavior in $Q(v_p)$ is a result of the change of the dominant dissipative mechanism of the unfolding process. At low pulling rates, $v_p < v_p^*$, friction is

negligible and energy is predominantly dissipated at the interface, reflecting the dissipative nature of the Arrhenius kinetics. At higher pulling rates, $v_p > v_p^*$, the energy dissipated due to friction between the molecule and its environment becomes dominant. Our results suggest that in our longest simulations at the smallest pulling rates, the two sources of dissipation compete with friction being larger.

6   Summary and discussion

Coiled-coils, present in major force-bearing cellular structures and in engineered biomaterials, exhibit an unfolding mechanism that allows them to sustain large strains and is critical for their biological function. Two-state models based on the Arrhenius law are popular to understand the unfolding mechanics of proteins in general, and of coiled-coils in particular. However, two-state models are unable to reproduce the mechanics of unfolding at high pulling rates, leading to the speculation that a different unfolding mechanism could become operative during highly out-of-equilibrium pulling regimes. Our combined all-atom MD/continuum theoretical study puts forth an alternative scenario, according to which the two-states picture and Arrhenius law are still valid at the interface, but the force at the interface driving the transition between the coiled and the unfolded states is significantly modified at high strain-rates by the friction between the protein and its environment. The pulling rates employed here (m/s) are still far from those that can be achieved by high-speed force spectroscopy (mm/s)[42]. Nevertheless, this high strain rate regime may be relevant in different scenarios, such when cells or artificial materials subjected to impact or blasts.

Our atomistically-informed continuum model of a phase-transforming rod describes the unfolding process across different regimes with a unique mechanism. It shows that friction attenuates the force exerted at the end of the protein along the fibril axis, an effect that increases with the pulling force. The model accurately predicts force-strain curves from MD simulations, corrects the Arrhenius law in terms of the applied force, and allows us to compute the energy dissipated during unfolding. We observe that coiled-coils dissipate small quantities of energy for small pulling rates, in agreement with previous works suggesting that they behave as truly elastic structures, but dissipate high amounts of energy for higher pulling rates, where they may act as shock absorbers. At high pulling rates, dissipation is dominated by friction, whereas at low pulling rates, it is dominated by the motion of the phase boundaries between the coiled and the unfolded phases. By identifying the previously unnoticed role of friction between the protein and its environment, our work may help rationalize out-of-equilibrium MD simulations and single molecule force spectroscopy experiments at high pulling rates, not only of coiled-coils but also of other fibrous proteins including single α-helical proteins.

Appendix A Molecular dynamics simulations

To understand the unfolding of coiled-coils under force, we performed molecular dynamics (MD) simulations of an artificial double-stranded coiled-coil made of two parallel α-helices, each with the amino acid sequence E(IEALKAE)$_{17}$IEA. Such an amino acid sequence has been shown experimentally to form coiled-coils that are very temperature and chemically stable even for short protein lengths[4,47]. The positions of the protein backbone atoms were obtained from the crystal structure of the myosin coiled-coil[25] with the amino acid sidechains replaced using the UCSF Chimera package[71]. The resulting coiled-coil ($\approx$18 nm long) was solvated with SPC water molecules[72] within a simulation box that could accommodate the completely unfolded protein ($\approx$ 45 nm long).

All MD simulations were performed with the GROMACS package version 4.5.5[73]. The coiled-coil protein is modeled with the GROMOS-54A7 force field[74]. The temperature was held constant at 310 K with a Nose-Hoover thermostat and the simulation box was held constant. Sodium and chloride ions were also added to neutralize the protein charge as well as provide physiological salt conditions. Following previous works[34–36,48], we pull from both ends of the protein at a fixed rate or with constant force. Harmonic restraints were used to keep the coiled-coils long axis aligned with the long dimension of the simulation box throughout all simulations.

Appendix B Onsager's formalism applied to phase-transforming rods

The governing equations of the phase transforming rod introduced in section 4 can be derived from a variational principle, called Onsager's variational principle. This general framework for the modeling of dissipative systems can be applied to low Reynols hydrodynamics, visco-elasticity, or chemical reactions among others[54,56,68]. Let us first introduced this principle for a simple 1D elastic rod embedded in a viscous fluid. A key ingredient in Onsager's principle is the free energy, which for an elastic rod of reference length L takes the simple form

$$A[\varphi_t] = \int_0^L f(\varepsilon) dX, \qquad (24)$$

where $\varepsilon = \partial_X \varphi_t(X) - 1$ is the strain, $\varphi_t(X)$ is the deformation mapping, f is the elastic energy density and $[\cdot]$ indicates a functional dependence. Another essential ingredient in Onsager's principle is the dissipation potential, which for viscous friction takes the form

$$D[\partial_t \varphi_t] = \int_0^L \frac{\eta}{2} \left(\partial_t \varphi_t \right)^2 dX, \qquad (25)$$

where η is the friction coefficient. We note that, while A depends functionally on φ_t, D depends on its time derivative $\partial_t \varphi_t$. This reflects that the free energy only depends on the state of the system, regardless of how the system reached that state. On the other hand, dissipation depends on how the system is changing its state. If a force F_a is applied between the ends of the protein, a power is added to the system

$$P[\partial_t \varphi_t] = F_a \left[\partial_t \varphi_t \right]_{X=0}^{X=L}. \qquad (26)$$

Onsager's principle then states that the dynamics of the system are given by

$$\partial_t \varphi_t = \underset{V}{\arg\min}\ \mathscr{R}[\varphi_t; V], \qquad (27)$$

where $\mathscr{R}$ is the Rayleghian,

$$\mathscr{R}[\varphi_t, \partial_t \varphi_t] = \dot{A}[\varphi_t, \partial_t \varphi_t] + D[\varphi_t, \partial_t \varphi_t] + P[\varphi_t, \partial_t \varphi_t], \qquad (28)$$

and $\dot{A}$ is the time-derivative of the free energy,

$$\begin{aligned}
\dot{A}[\varphi_t; \partial_t \varphi_t] &= \int_0^L f'(\varepsilon) \partial_X \partial_t \varphi_t dX \\
&= -\int_0^L \partial_X f'(\varepsilon) \partial_t \varphi_t dX + \left[f'(\varepsilon) \partial_t \varphi_t \right]_{X=0}^{X=L},
\end{aligned} \qquad (29)$$

where we have integrated by parts. Defining the stress $F(\varepsilon) = f'(\varepsilon)$, the equations resulting from the minimization are

$$\partial_X F(\varepsilon) = \eta \partial_t \varphi_t, \qquad \text{for } 0 < X < L \qquad (30)$$

$$F_a = F(\varepsilon), \qquad \text{for } X = 0 \text{ or } X = L. \qquad (31)$$

We now look at the variational formulation of a phase-transforming rod deforming in a viscous fluid. We consider that $f(\varepsilon)$ is characterized by two quadratic functions in either of the phases and that the system presents two interfaces, characterized by positions S_1 and S_2. In this case, the free energy is

$$\begin{aligned}
A[\varphi_t, S_1, S_2] &= \int_0^{S_1} \left[k_{\text{un}} \left(\varepsilon - \varepsilon_{\text{un}}^0 \right)^2 + \Delta a \right] dX + \int_{S_1}^{S_2} k_{\text{co}} \varepsilon^2 dX \\
&\quad + \int_{S_2}^L \left[k_{\text{un}} \left(\varepsilon - \varepsilon_{\text{un}}^0 \right)^2 + \Delta a \right] dX.
\end{aligned} \qquad (32)$$

where apart from φ_t, A also depends on the positions of the interfaces S_1 and S_2 to characterize the system. Here $\Delta a = F_0 \varepsilon_{\text{un}}^0$ identifies the difference in free energy density between the unfolded and coiled states at equilibrium. Dissipation now takes the form

$$\begin{aligned}
D[\varphi_t, S_1, S_2; \partial_t \varphi_t, \dot{S}_1, \dot{S}_2] &= \int_0^{S_1} \frac{\eta_{\text{un}}}{2} v^2 dX + \int_{S_1}^{S_2} \frac{\eta_{\text{co}}}{2} v^2 dX \\
&\quad + \int_{S_2}^L \frac{\eta_{\text{un}}}{2} v^2 dX + \frac{1}{2\bar{\kappa}_1} \dot{S}_1^2 + \frac{1}{2\bar{\kappa}_2} \dot{S}_2^2,
\end{aligned} \qquad (33)$$

where $\bar{\kappa}_2$ and $\bar{\kappa}_1$ characterize the dissipation generated by the propagation of the interfaces; these are non-linear functions of the deformation, as will become clear later. Again, we consider the power input

$$P[\partial_t \varphi_t] = F_a \left[\partial_t \varphi_t \right]_{X=0}^{X=L}. \qquad (34)$$

Towards applying Onsager's principle, we compute the rate of change of the free energy

$$
\dot{A} = -\int_0^{S_1} k \partial_X^2 \varphi_t \partial_t \varphi_t dX + \left[k \left(\partial_X \varphi_t - 1 - \varepsilon_{\mathrm{un}}^0 \right) \partial_t \varphi_t \right]_{X=0}^{X=S_1}
$$

$$
- \int_{S_1}^{S_2} k \partial_X^2 \varphi_t \partial_t \varphi_t dX + \left[(\partial_X \varphi_t - 1) \partial_t \varphi_t \right]_{X=S_1}^{X=S_2}
$$

$$
- \int_{S_2}^{L} k \partial_X^2 \varphi_t \partial_t \varphi_t dX + \left[k \left(\partial_X \varphi_t - 1 - \varepsilon_{\mathrm{un}}^0 \right) \partial_t \varphi_t \right]_{X=S_2}^{X=L} \quad (35)
$$

$$
+ \left[k_{\mathrm{co}} (\partial_X \varphi_t - 1)^2 - k_{\mathrm{un}} \left(\partial_X \varphi_t - 1 - \varepsilon_{\mathrm{un}}^0 \right)^2 - \Delta a \right] \dot{S}_2
$$

$$
- \left[k_{\mathrm{co}} (\partial_X \varphi_t - 1)^2 - k_{\mathrm{un}} \left(\partial_X \varphi_t - 1 - \varepsilon_{\mathrm{un}}^0 \right)^2 - \Delta a \right] \dot{S}_1
$$

Again, Onsager's principle states that the dynamics minimizes the Rayleighian

$$
\mathscr{R}[\varphi_t, S_1, S_2; \partial_t \varphi_t, \dot{S}_1, \dot{S}_2] = \dot{A}[\varphi_t, S_1, S_2; \partial_t \varphi_t, \dot{S}_1, \dot{S}_2] + P[\partial_t \varphi_t]
$$
$$
+ D[\varphi_t, S_1, S_2; \partial_t \varphi_t, \dot{S}_1, \dot{S}_2]. \quad (36)
$$

Mathematically,

$$
\{ \partial_t \varphi_t, \dot{S}_1, \dot{S}_2 \} = \underset{V, T_1, T_2}{\arg\min} \mathscr{R}[\varphi_t, S_1, S_2; V, T_1, T_2]. \quad (37)
$$

The resulting equations are

$$
\partial_X F(X, t) = \eta \partial_t \varphi_t, \quad (38)
$$

with

$$
F(X, t) = \begin{cases} k_{\mathrm{co}} (\partial_X \varphi_t - 1) & \text{if } S_1 < X < S_2 \\ k_{\mathrm{un}} (\partial_X \varphi_t - 1 - \varepsilon_{\mathrm{un}}^0) & \text{otherwise} \end{cases} \quad (39)
$$

As before, the applied force is

$$
F_a = k_{\mathrm{un}} \partial_X \varphi_t, \quad \text{for } X = 0 \text{ or } X = L. \quad (40)
$$

and the force at the interfaces

$$
F_{S_i} = k_{\mathrm{co}} (\partial_X \varphi_t - 1) = k_{\mathrm{un}} \left(\partial_X \varphi_t - 1 - \varepsilon_{\mathrm{un}}^0 \right), \quad \text{at } X = S_i. \quad (41)
$$

The movement of the interfaces is given by

$$
\dot{S}_i = (-1)^i \bar{\kappa} \left(\Delta a - \varepsilon_{\mathrm{un}}^0 F_{S_i} \right). \quad (42)
$$

To match this expression with Arrhenius law

$$
\dot{S}_i = (-1)^{i-1} k_0 \left[\exp\left(-\frac{G_b^+(F_{S_i})}{k_B T} \right) - \exp\left(-\frac{G_b^-(F_{S_i})}{k_B T} \right) \right], \quad (43)
$$

we identify

$$
\bar{\kappa}_i = k_0 \frac{\exp\left(-\dfrac{G_b^+(F_{S_i})}{k_B T} \right) - \exp\left(-\dfrac{G_b^-(F_{S_i})}{k_B T} \right)}{\left(\varepsilon_{\mathrm{un}}^0 F_{S_i} - \Delta a \right)}. \quad (44)
$$

Note that since both numerator and denominator change sign at the Maxwell force $F_{S_i} = F_0$, $\bar{\kappa}_i$ is always positive, leading to a positive dissipation in agreement with the second law of thermodynamics.

Appendix C   Numerical integration of the continuum model

To simulate our one-dimensional continuum model, we discretize the reference domain in space using a finite difference setting with an evenly distributed set of N nodes $\{X_1, X_2, \ldots, X_N\}$ with inter-node distance $\Delta = L/(N-1)$. We denote by $\{x_1, x_2, \ldots, x_N\}$ their positions in the deformed configuration. Then, Eq. (13) can be discretized as

$$
\frac{dx^i}{dt} = \frac{F^{i+\frac{1}{2}} - F^{i-\frac{1}{2}}}{\Delta \cdot \eta}, \quad (45)
$$

where

$$
F^{i+\frac{1}{2}} = \begin{cases} k_{\mathrm{co}} \left(\dfrac{x^{i+1} - x^i}{\Delta} - 1 \right), & \text{if } X_i > S_1 \text{ and } X_{i+1} < S_2, \\[3mm] k_{\mathrm{un}} \left(\dfrac{x^{i+1} - x^i}{\Delta} - 1 - \varepsilon_{\mathrm{un}}^0 \right), & \text{if } X_{i+1} < S_1 \text{ or } X_i > S_2. \end{cases} \quad (46)
$$

Note, however, that these equations do not include the movement of the interfaces S_1 and S_2 or the nodes next to them. To represent propagating phase boundaries we follow the approach by Raj and Purohit[61, 75] and follow them with two additional nodes, of position S_1 and S_2, that move along the reference configuration. Across these moving nodes, ε can be discontinuous. Let us assume that, at time t, S_2 lies between nodes u and $u+1$. In this case, the segment $\overline{X_u S_2}$, with reference length $\Delta_{\mathrm{co}} = S_2 - X_u$, is in the coiled state and the segment $\overline{X_u S_2}$, with reference length $\Delta_{\mathrm{un}} = X_{u+1} - S_2$, is in the unfolded state. Δ_{co} and Δ_{un} are related through

$$
\Delta = \Delta_{\mathrm{co}} + \Delta_{\mathrm{un}}. \quad (47)
$$

Let us denote by F_{co} the stress at the interface in the coiled phase and by F_{un} the stress at the interface in the unfolded phase. Balance of linear momentum at the interface requires that the stress is continuous $F_{\mathrm{co}} - F_{\mathrm{un}} = 0$, i.e.

$$
F_{\mathrm{co}} - F_{\mathrm{un}} = k_{\mathrm{co}} \varepsilon_{\mathrm{co}} - k_{\mathrm{un}} (\varepsilon_{\mathrm{un}} - \varepsilon_{\mathrm{un}}^0) = 0, \quad (48)
$$

where $\varepsilon_{\mathrm{co}}$ and $\varepsilon_{\mathrm{un}}$ are the strains of the segments $\overline{X_u S_2}$ and $\overline{S_2 X_{u+1}}$ at time t respectively. Furthermore, from the continuity of $\varphi_t(X)$ we have

$$
(\varepsilon_{\mathrm{co}} + 1)\Delta_{\mathrm{co}} + (\varepsilon_{\mathrm{un}} + 1)\Delta_{\mathrm{un}} = x_{u+1} - x_u. \quad (49)
$$

Assuming the position of S_2 at time t is given, Eqs. (48) and (49) can be solved for $\varepsilon_{\mathrm{co}}$ and $\varepsilon_{\mathrm{un}}$. The force at the interface at time t is then given by $F_{S_2} = k_{\mathrm{co}} \varepsilon_{\mathrm{co}} = k_{\mathrm{un}} (\varepsilon_{\mathrm{un}} - \varepsilon_{\mathrm{un}}^0)$, which determines the interface velocity from Eq. (4), i.e.

$$
\dot{S}_2 = -\frac{k_0 L}{2} \left(e^{-G_b^+(F_{S_2})/k_B T} - e^{-G_b^-(F_{S_2})/k_B T} \right). \quad (50)
$$

Parameter	Value
η	8 pN·ns/nm^2
k_{co}	4.4×10^3 pN
k_{un}	5.0×10^3 pN
$\varepsilon_{\mathrm{un}}^0$	1.15
k_0	3.8×10^9 m/s
F_0	113 pN
A	74.96 kJ/mol
$p_{\leftarrow}^{+}$	-0.4×10^{-1} kJ/(mol·pN)
$p_{\rightarrow}^{+}$	-0.8×10^{-1} kJ/(mol·pN)
$p_{\leftarrow}^{-}$	1.5×10^{-1} kJ/(mol·pN)
$p_{\rightarrow}^{-}$	1.1×10^{-1} kJ/(mol·pN)

Table 1 Parameters for the continuum model

To compute the time-evolution of the nodes next to the interface, we discretize Eq. (13) as

$$\frac{dx^u}{dt} = \frac{F_{S_2} - F^{u-\frac{1}{2}}}{\eta(\Delta/2 + \Delta_{\mathrm{co}})}, \tag{51}$$

$$\frac{dx^{u+1}}{dt} = \frac{F^{u+\frac{3}{2}} - F_{S_2}}{\eta(\Delta/2 + \Delta_{\mathrm{un}})}. \tag{52}$$

Following an identical procedure, one finds $\dot{S}_1$ and the ODEs dictating the evolution of the nodes next to it. Eqs. (45), (50), (51), and (52), along with the corresponding equations for the first interface, form a coupled set of ordinary differential equations, which we solve using the LSODA solver part of the ODEPACK library as implemented in the Scipy package[76].

The previous equations depend on the functions $G_b^+(F)$ and $G_b^-(F)$. These functions do not seem to obey a simple law for the whole range of forces, but they can be linearized above and below the transition separately, obtaining

$$G_b^+(F) = \begin{cases} A + p_{\leftarrow}^{+}(F - F_0) & \text{if } F > F_0, \\ A + p_{\rightarrow}^{+}(F - F_0) & \text{if } F \leq F_0, \end{cases} \tag{53}$$

and

$$G_b^-(F) = \begin{cases} A + p_{\leftarrow}^{-}(F - F_0) & \text{if } F > F_0, \\ A + p_{\rightarrow}^{-}(F - F_0) & \text{if } F \leq F_0, \end{cases} \tag{54}$$

where the parameters A and $p_{\leftrightarrow}^{\pm}$ are listed in Table 1.

References

1 A. Rose and I. Meier, *Cell. Mol. Life Sci.*, 2004, **61**, 1996–2009.

2 E. Wolf, P. S. Kim and B. Berger, *Protein Sci.*, 1997, **6**, 1179–1189.

3 F. H. C. Crick, *Acta Crystallogr.*, 1953, **6**, 689–697.

4 B. Apostolovic, M. Danial and H.-A. Klok, *Chem. Soc. Rev.*, 2010, **39**, 3541–3575.

5 P. Burkhard, J. Stetefeld and S. V. Strelkov, *Trends Cell Biol.*, 2001, **11**, 82–88.

6 J. M. Mason and K. M. Arndt, *Chembiochem*, 2004, **5**, 170–176.

7 D. D. Root, V. K. Yadavalli, J. G. Forbes and K. Wang, *Biophys. J.*, 2006, **90**, 2852–2866.

8 I. Schwaiger, C. Sattler, D. R. Hostetter and M. Rief, *Nat. Mater.*, 2002, **1**, 232–235.

9 S. M. Kreuzer and R. Elber, *Biophys. J.*, 2013, **105**, 951–961.

10 J. E. Eriksson, T. Dechat, B. Grin, B. Helfand, M. Mendez, H.-M. Pallari and R. D. Goldman, *J. Clin. Invest.*, 2009, **119**, 1763–1771.

11 H. Herrmann, H. Bär, L. Kreplak, S. V. Strelkov and U. Aebi, *Nat. Rev. Mol. Cell Biol.*, 2007, **8**, 562–573.

12 B. Alberts, A. Johnson, J. Lewis, D. Morgan, M. Raff, K. Roberts and P. Walter, *Molecular Biology of the Cell, Sixth Edition*, Garland Science, 2014.

13 Z. Qin, L. Kreplak and M. J. Buehler, *PLoS One*, 2009, **4**, e7294.

14 P. a. Janmey, U. Euteneuer, P. Traub and M. Schliwa, *J. Cell Biol.*, 1991, **113**, 155–160.

15 D. Fudge, D. Russell, D. Beriault, W. Moore, E. B. Lane and a. W. Vogl, *PLoS One*, 2008, **3**, e2327.

16 N. Wang, J. P. Butler and D. E. Ingber, *Science*, 1993, **260**, 1124–1127.

17 N. Wang and D. Stamenovic, *J. Muscle Res. Cell Motil.*, 2002, **23**, 535–540.

18 L. Kreplak, H. Herrmann and U. Aebi, *Biophys. J.*, 2008, **94**, 2790–2799.

19 Z. Qin, M. J. Buehler and L. Kreplak, *J. Biomech.*, 2010, **43**, 15–22.

20 E. Latorre, S. Kale, L. Casares, M. Gómez-González, M. Uroz, L. Valon, R. V. Nair, E. Garreta, N. Montserrat, A. del Campo, B. Ladoux, M. Arroyo and X. Trepat, *Nature*, 2018, **563**, 203–208.

21 J. Block, H. Witt, A. Candelli, E. J. G. Peterman, G. J. L. Wuite, A. Janshoff and S. Köster, *Phys. Rev. Lett.*, 2017, **118**, 048101.

22 R. L. C. Akkermans and P. B. Warren, *Philos. Trans. A Math. Phys. Eng. Sci.*, 2004, **362**, 1783–1793.

23 J. W. Hearle, *Int. J. Biol. Macromol.*, 2000, **27**, 123–138.

24 M. Feughelman, *J. Appl. Polym. Sci.*, 2002, **83**, 489–507.

25 W. Blankenfeldt, N. H. Thomä, J. S. Wray, M. Gautel and I. Schlichting, *Proc. Natl. Acad. Sci. U. S. A.*, 2006, **103**, 17713–17717.

26 a. M. Lauzon, P. M. Fagnant, D. M. Warshaw and K. M. Trybus, *Biophys. J.*, 2001, **80**, 1900–1904.

27 D. N. Woolfson, *Biopolymers*, 2010, **94**, 118–127.

28 C. Xu, R. Liu, A. K. Mehta, R. C. Guerrero-Ferreira, E. R. Wright, S. Dunin-Horkawicz, K. Morris, L. C. Serpell, X. Zuo, J. S. Wall and V. P. Conticello, *J. Am. Chem. Soc.*, 2013, **135**, 15565–15578.

29 N. C. Burgess, T. H. Sharp, F. Thomas, C. W. Wood, A. R. Thomson, N. R. Zaccai, R. L. Brady, L. C. Serpell and D. N. Woolfson, *J. Am. Chem. Soc.*, 2015, **137**, 10554–10562.

30 J. Kopecek, *Biomaterials*, 2007, **28**, 5185–5192.

31 E. F. Banwell, E. S. Abelardo, D. J. Adams, M. A. Birchall, A. Corrigan, A. M. Donald, M. Kirkland, L. C. Serpell, M. F. Butler and D. N. Woolfson, *Nat. Mater.*, 2009, **8**, 596–600.

32 V. Conticello, S. Hughes and C. Modlin, in *Fibrous Proteins:*

Structures and Mechanisms, ed. D. A. D. Parry and J. M. Squire, Springer, Cham, Cham, 2017, vol. 82 of Subcellular Biochemistry, pp. 575–600.

33 A. E. X. Brown, R. I. Litvinov, D. E. Discher and J. W. Weisel, *Biophys. J.*, 2007, **92**, L39–41.

34 T. Ackbarow and M. J. Buehler, *J. Mater. Sci.*, 2007, **42**, 8771–8787.

35 T. Ackbarow, X. Chen, S. Keten and M. J. Buehler, *Proc. Natl. Acad. Sci. U. S. A.*, 2007, **104**, 16410–16415.

36 K. A. Minin, A. Zhmurov, K. A. Marx, P. K. Purohit and V. Barsegov, *J. Am. Chem. Soc.*, 2017, **139**, 16168–16177.

37 H. A. Kramers, *Physica*, 1940, **7**, 284–304.

38 G. I. Bell, *Science*, 1978, **200**, 618–627.

39 E. Evans and K. Ritchie, *Biophys. J.*, 1997, **72**, 1541–1555.

40 M. Gao, H. Lu and K. Schulten, *J. Muscle Res. Cell Motil.*, 2002, **23**, 513–521.

41 M. Sotomayor and K. Schulten, *Science*, 2007, **316**, 1144–1148.

42 F. Rico, L. Gonzalez, I. Casuso, M. Puig-Vidal and S. Scheuring, *Science*, 2013, **342**, 741–743.

43 J. E. Burda, A. M. Bernstein and M. V. Sofroniew, *Experimental Neurology*, 2016, **275**, 305 – 315.

44 A. E. Bergues-Pupo, K. G. Blank, R. Lipowsky and A. Vila Verde, *Phys. Chem. Chem. Phys.*, 2018, **20**, 29105–29115.

45 M. Goktas, C. Luo, R. M. A. Sullan, A. E. Bergues-Pupo, R. Lipowsky, A. Vila Verde and K. G. Blank, *Chem. Sci.*, 2018, **9**, 4610–4621.

46 Z. Qin and M. J. Buehler, *Phys. Rev. Lett.*, 2010, **104**, 198304.

47 J. Y. Su, R. S. Hodges and C. M. Kay, *Biochemistry*, 1994, **33**, 15501–15510.

48 A. Zhmurov, O. Kononova, R. I. Litvinov, R. I. Dima, V. Barsegov and J. W. Weisel, *J. Am. Chem. Soc.*, 2012, **134**, 20396–20402.

49 Y. Taniguchi, B. S. Khatri, D. J. Brockwell, E. Paci and M. Kawakami, *Biophys. J.*, 2010, **99**, 257–262.

50 J. H. Gibbs and E. A. DiMarzio, *J. Chem. Phys.*, 1958, **28**, 1247–1248.

51 C. Kittel, *Am. J. Phys.*, 1969, **37**, 917–920.

52 R. Zwanzig, *Proc. Natl. Acad. Sci. U. S. A.*, 1997, **94**, 148–150.

53 I. L. Jäger, *Biophys. J.*, 2001, **81**, 1897–1906.

54 L. Onsager, *Phys. Rev.*, 1931, **37**, 405–426.

55 H. B. Callen, *Thermodynamics & an Intro. to Thermostatistics*, John wiley & sons, 2006.

56 M. Doi, *J. Phys. Condens. Matter*, 2011, **23**, 284118.

57 S. O. Samuelson, G. J. Martyna and I. Introduction, *J. Chem. Phys.*, 1998, **109**, 11061–11073.

58 A. Barducci, G. Bussi and M. Parrinello, *Phys. Rev. Lett.*, 2008, **100**, 020603.

59 P. Raiteri, A. Laio, F. L. Gervasio, C. Micheletti and M. Parrinello, *J. Phys. Chem. B*, 2006, **110**, 3533–3539.

60 M. Bonomi, D. Branduardi, G. Bussi, C. Camilloni, D. Provasi, P. Raiteri, D. Donadio, F. Marinelli, F. Pietrucci, R. A. Broglia and M. Parrinello, *Comput. Phys. Commun.*, 2009, **180**, 1961–1972.

61 R. Raj and P. K. Purohit, *J. Mech. Phys. Solids*, 2011, **59**, 2044–2069.

62 Q. Zhao and P. K. Purohit, *Int. J. Solids Struct.*, 2016, **94-95**, 238–246.

63 M. Arroyo and I. Arias, *J. Mech. Phys. Solids*, 2008, **56**, 1224–1244.

64 I. Benichou and S. Givli, *J. Mech. Phys. Solids*, 2013, **61**, 94–113.

65 A. Miserez, S. S. Wasko, C. F. Carpenter and J. H. Waite, *Nat. Mater.*, 2009, **8**, 910–916.

66 F. D. Fischer, M. J. Harrington and P. Fratzl, *New J. Phys.*, 2013, **15**, 065004.

67 C. Brennen and H. Winet, *Annu. Rev. Fluid Mech.*, 1977, **9**, 339–398.

68 M. Arroyo, N. Walani, A. Torres-Sánchez and D. Kaurin, in *The Role of Mechanics in the Study of Lipid Bilayers*, ed. D. J. Steigmann, Springer International Publishing, Cham, 2018, pp. 287–332.

69 A. Torres-Sánchez, J. M. Vanegas and M. Arroyo, *Phys. Rev. Lett.*, 2015, **114**, 258102.

70 A. Torres-Sánchez, J. M. Vanegas and M. Arroyo, *J. Mech. Phys. Solids*, 2016, **93**, 224–239.

71 E. F. Pettersen, T. D. Goddard, C. C. Huang, G. S. Couch, D. M. Greenblatt, E. C. Meng and T. E. Ferrin, *J. Comput. Chem.*, 2004, **25**, 1605–1612.

72 H. J. C. Berendsen, J. P. M. Postma, W. F. van Gunsteren and J. Hermans, in *Intermolecular Forces*, ed. B. Pullman, Reidel, Dordrecht, 1981, pp. 331–342.

73 S. Pronk, S. Páll, R. Schulz, P. Larsson, P. Bjelkmar, R. Apostolov, M. R. Shirts, J. C. Smith, P. M. Kasson, D. van der Spoel, B. Hess and E. Lindahl, *Bioinformatics*, 2013, **29**, 845–854.

74 N. Schmid, A. P. Eichenberger, A. Choutko, S. Riniker, M. Winger, A. E. Mark and W. F. van Gunsteren, *Eur. Biophys. J.*, 2011, **40**, 843–856.

75 R. Raj and P. K. Purohit, *EPL*, 2010, **91**, 28003.

76 E. Jones, T. Oliphant and P. Peterson, *SciPy: Open source scientific tools for Python*, http://www.scipy.org/, 2001.